Extremely Dense Gamma-Ray Pulses in Electron Beam-Multifoil Collisions

Archana Sampath,[1] Xavier Davoine,[2,3] Sébastien Corde,[4] Laurent Gremillet,[2,3] Maitreyi Sangal,[1] Christoph H. Keitel,[1] Robert Ariniello,[5] John Cary,[5] Henrik Ekerfelt,[6] Claudio Emma,[6] Frederico Fiuza,[6] Hiroki Fujii,[7] Max Gilljohann,[4] Mark Hogan,[6] Chan Joshi,[7] Alexander Knetsch,[4] Olena Kononenko,[4] Valentina Lee,[5] Mike Litos,[5] Kenneth Marsh,[7] Zan Nie,[7] Brendan O'Shea,[6] J. Ryan Peterson,[6,8] Pablo San Miguel Claveria,[4] Doug Storey,[6] Yipeng Wu,[7] Xinlu Xu,[6] Chaojie Zhang,[7] and Matteo Tamburini[1,*]

[1] *Max-Planck-Institut für Kernphysik, Saupfercheckweg 1, D-69117 Heidelberg, Germany*
[2] *CEA, DAM, DIF, 91297 Arpajon, France*
[3] *Université Paris-Saclay, CEA, LMCE, 91680 Bruyères-le-Châtel, France*
[4] *LOA, ENSTA Paris, CNRS, Ecole Polytechnique, Institut Polytechnique de Paris, 91762 Palaiseau, France*
[5] *University of Colorado Boulder, Department of Physics, Center for Integrated Plasma Studies, Boulder, Colorado 80309, USA*
[6] *SLAC National Accelerator Laboratory, Menlo Park, CA 94025, USA*
[7] *University of California Los Angeles, Los Angeles, CA 90095, USA*
[8] *Stanford University, Physics Department, Stanford, CA 94305, USA*

(Dated: September 28, 2020)

Sources of high-energy photons have important applications in almost all areas of research. However, the photon flux and intensity of existing sources is strongly limited for photon energies above a few hundred keV. Here we show that a high-current ultrarelativistic electron beam interacting with multiple submicrometer-thick conducting foils can undergo strong self-focusing accompanied by efficient emission of gamma-ray synchrotron photons. Physically, self-focusing and high-energy photon emission originate from the beam interaction with the near-field transition radiation accompanying the beam-foil collision. This near field radiation is of amplitude comparable with the beam self-field, and can be strong enough that a single emitted photon can carry away a significant fraction of the emitting electron energy. After beam collision with multiple foils, femtosecond collimated electron and photon beams with number density exceeding that of a solid are obtained. The relative simplicity, unique properties, and high efficiency of this gamma-ray source open up new opportunities both for applied and fundamental research including laserless investigations of strong-field QED processes with a single electron beam.

Intense sources of high-energy photons have broad applications in industry, medicine, materials science [1–4] as well as in nuclear physics, particle physics and laboratory astrophysics [5–7]. This large variety of applications motivated the construction of numerous facilities worldwide from synchrotrons and FELs [4, 8], which provide bright sources of photons with energies up to some hundred keV, to Compton-based facilities aiming at photon energies up to 20 MeV [7].

Recently, the growing interest in intense high-energy photon sources has stimulated several proposals to further increase the attainable photon energy and flux. These proposals include high-power laser-plasma interaction [9–21], plasma instabilities [22], QED cascades [23, 24], multiple colliding laser pulses [25, 26] and beamstrahlung [27–29]. A number of experiments, where the generated photon beam properties could be accurately measured and tuned, were also successfully performed [30–37]. However, the attainable density of collimated gamma-ray beams remains less than $\sim 10^{24}$ m^{-3}.

The investigation of exotic phenomena such as light-by-light scattering, birefringence and dichroism of the quantum vacuum, catalytic generation of electron-positron cascades by high-energy photons, quark-gluon physics as well as the creation of dense electron-positron plasmas for laboratory astrophysics would greatly benefit from substantial enhancements of the density of multi-MeV photon sources to solid density levels (10^{29} particles/m^3) [6, 38–40].

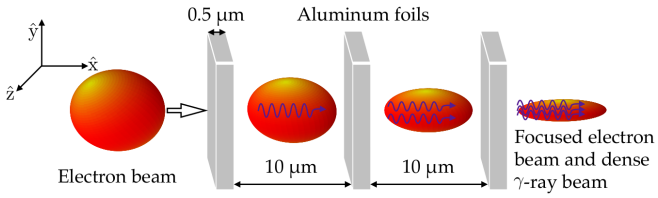

FIG. 1. Schematic setup. An ultrarelativistic electron beam sequentially collides with aluminum foils. At each beam-foil collision, a strong transverse force which focuses the electron beam and leads to copious gamma-ray emission is induced.

To this goal, here we introduce a novel concept for an ultraintense gamma-ray source based on the interaction of a single high-current ultrarelativistic electron beam with multiple submicrometer-thick conducting foils (see Fig. 1). By using fully 3D particle-in-cell (PIC) simulations, we show that: (i) An ultrarelativistic (10 GeV), dense (4.7×10^{27} m^{-3}) electron beam can be radially focused up to 3.8×10^{29} m^{-3}, i.e., beyond

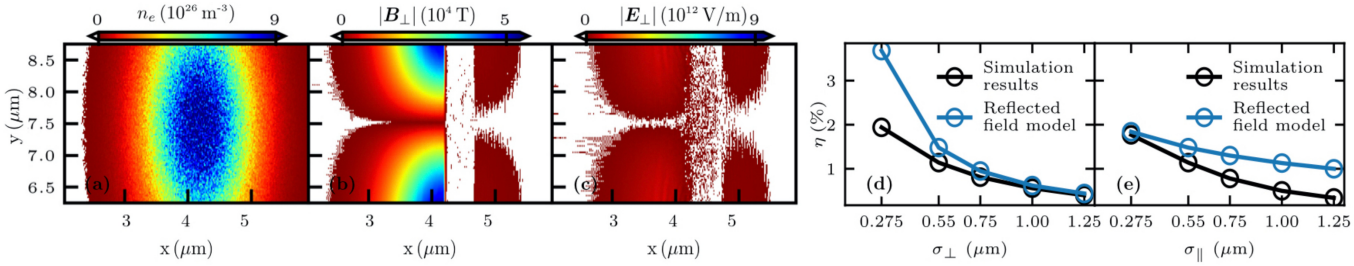

FIG. 2. (a) Electron beam density, (b) transverse magnetic field, and (c) transverse electric field in the collision with a 0.5μm-thick aluminum foil. For comparison, the magnetic and electric beam self-fields are 3.1×10^4 T, and 9.4×10^{12} V/m, respectively. (d) Electron beam to radiation energy conversion efficiency η as a function of $\sigma_\perp$ in the collision with one foil. The electron beam has 2 nC charge, 10 GeV energy, and $\sigma_\parallel = 0.55$ μm. Black circles: 3D PIC simulations results; blue circles: reflected-beam model predictions. (e) Same as in panel (d) but for $\sigma_\perp = 0.55$ μm and as a function of $\sigma_\parallel$.

the 1.8×10^{29} m^{-3} electron density of solid aluminum; (ii) Electron beam focusing is accompanied by intense synchrotron photon emission with more than 30% of the electron beam energy converted into a 4.1×10^{29} m^{-3} peak density collimated gamma-ray beam; (iii) When the electron beam density exceeds the foil electron density, the beam self-fields expel the target electrons and create an electron-depleted channel through the foil. The fields experienced by the beam electrons inside the plasma channel are so high that the quantum parameter $\chi \approx \gamma|\boldsymbol{f}_\perp|/eF_{\rm cr}$ exceeds unity [41, 42]. Here $\boldsymbol{f}_\perp = q(\boldsymbol{E}_\perp + \boldsymbol{\beta} \times \boldsymbol{B})$ is the Lorentz force transverse to the beam velocity, γ is the beam relativistic factor, $q = -e$ is the electron charge, $F_{\rm cr} = m_e^2c^3/e\hbar \approx 1.3 \times 10^{18}$ V/m is the QED critical field [6, 41, 42]. This opens up the possibility of laserless strong-field QED investigations with only one ultrarelativistic electron beam [43].

We start by considering the free propagation of an electron beam in vacuum. The electric $\boldsymbol{E}$ and magnetic $\boldsymbol{B}$ self-fields of a cold electron beam in vacuum are related by $\boldsymbol{B} = \boldsymbol{\beta} \times \boldsymbol{E}$ [44], where $\boldsymbol{\beta} = \boldsymbol{v}/c$ is the normalized beam velocity (Gaussian units are employed for equations). Thus, $\boldsymbol{f}_\perp = q\boldsymbol{E}_\perp/\gamma^2$ is strongly suppressed for large γ, and the beam propagates almost ballistically over relatively long distances in vacuum.

When a beam collides with a conductor, it can be subject to strong near-field coherent transition radiation (CTR), which alters the nearly perfect cancellation of the electric and magnetic terms in the Lorentz force. Electromagnetic boundary conditions require that the electric field component tangential to the surface of a perfect conductor must be continuous and zero at the conductor surface, whereas the tangential magnetic field can be discontinuous and remains large [44]. Thus, when an electron beam encounters a conductor, the magnetic term of the Lorentz force, which drives beam focusing, can overcome the electric term, which drives beam expansion. Effectively, when the beam length is smaller than its transverse size, this process can be visualized as a beam colliding with its image charge (see below and Supplemental Material). Notice that a large $\boldsymbol{f}_\perp$ naturally results in intense emission of radiation. For instance, in the classical regime the radiated power (mean photon energy) is proportional to $\gamma^2\boldsymbol{f}_\perp^2$ ($\gamma^2\boldsymbol{f}_\perp$) [42, 44].

For modeling, we consider an ultrarelativistic cold electron beam with cylindrical symmetry around its propagation axis x. The description is simplified by employing cylindrical coordinates with $r = \sqrt{y^2 + z^2}$, $\theta = \arctan(z/y)$, and x being the radial, azimuthal and vertical components, respectively. We assume that cylindrical symmetry is preserved throughout the interaction. Hence, fields are independent of θ, the azimuthal electric field E_θ and the radial B_r and vertical B_x components of the magnetic field are zero. Here beam and conductor fields are denoted by the superscript b and c, respectively. For an ultrarelativistic charge distribution $\rho(x,r,t) = \rho_0 e^{-r^2/2\sigma_\perp^2} e^{-(x-x_0-vt)^2/2\sigma_\parallel^2}$ with N_e electrons, initial position x_0, velocity v along x, and peak charge density $\rho_0 = qN_e/(2\pi)^{3/2}\sigma_\perp^2\sigma_\parallel$, $E_r^b \gg E_x^b \approx 0$,

$$E_r^b(x,r,t) = \frac{2qN_e}{\sqrt{2\pi}\sigma_\parallel} \frac{(1 - e^{-r^2/2\sigma_\perp^2}) e^{-(x-x_0-vt)^2/2\sigma_\parallel^2}}{r}, \tag{1}$$

and $B_\theta^b(x,r,t) = \beta E_r^b(x,r,t)$, provide an approximate solution to Maxwell equations up to terms of order $1/\gamma^2$ around the beam [43]. To evaluate $E_r^c(x,r,t)$ and $B_\theta^c(x,r,t)$, we consider a flat perfectly conducting foil with front surface at $x = 0$. When the electron beam is outside the conductor, the method of images can be employed for determining $E_r^c(x,r,t)$ and $B_\theta^c(x,r,t)$ in $x < 0$ [45]. This method cannot be applied when the beam enters the foil, because the image would be located in $x < 0$, where conductor fields must satisfy source-free Maxwell equations. However, when $\sigma_\perp \gg \sigma_\parallel$ one can approximate $E_r^c(x,r,t)$ and $B_\theta^c(x,r,t)$ with the image charge fields. This "reflected' beam" approximation holds because CTR, which is emitted with transverse size $\sigma_\perp$ and typical wavelength $\sigma_\parallel$, undergoes weak diffraction over a Rayleigh length of approximately $\sigma_\perp^2/\sigma_\parallel \gg \sigma_\parallel$ from the boundary. The opposite limit $\sigma_\perp \ll \sigma_\parallel$, cor-

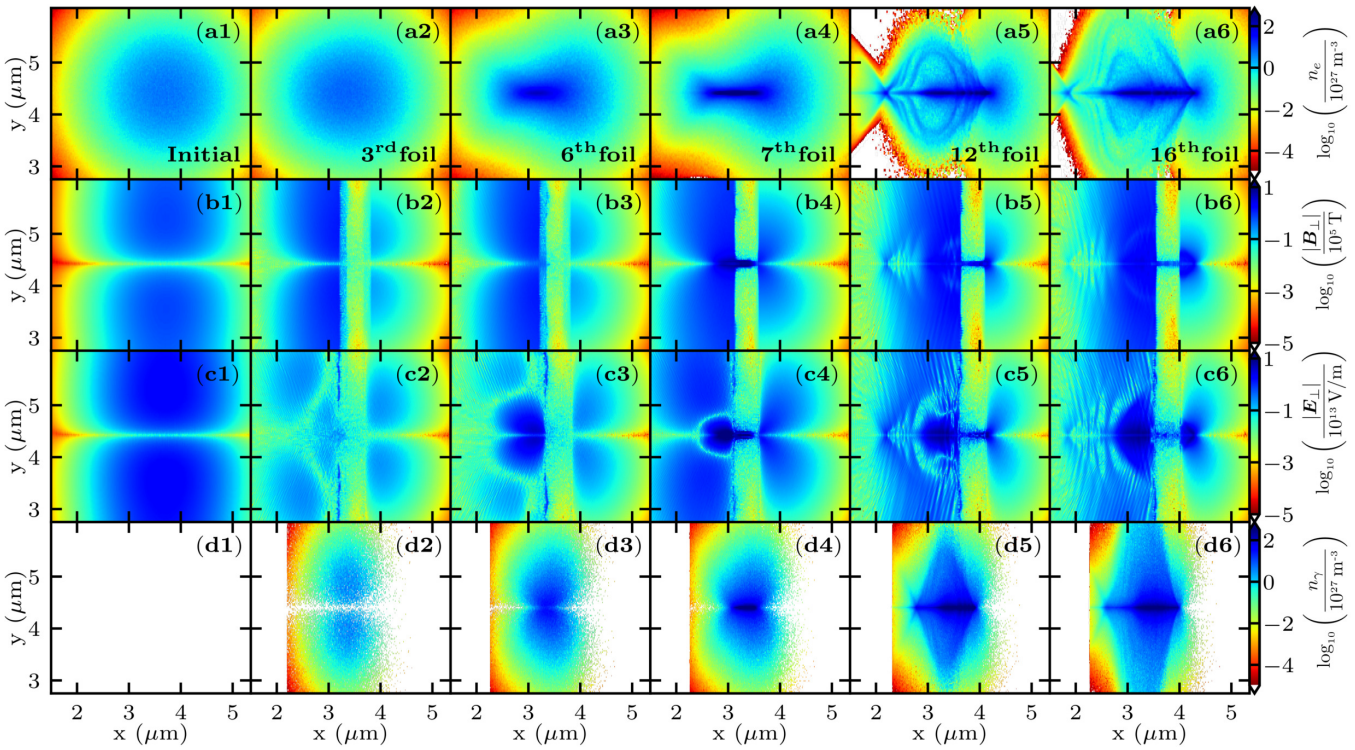

FIG. 3. Beam evolution. First column, initial electron beam density (a1), its magnetic (b1) and electric (c1) field, and the initial photon density (d1). Second to sixth column, same quantities as in the first column but at the 3rd (a2)-(d2), the 6th (a3)-(d3), the 7th (a4)-(d4), the 12th (a5)-(d5), and the 16th (a6)-(d6) beam-foil interaction, respectively.

responds to the magnetostatic approximation, yielding a vanishing B_θ^c and a surface-localized E_r^c (see Supplemental Material). Note that beam focusing in the $\sigma_\perp \ll \sigma_\parallel$ limit has been demonstrated in accelerators [46–50].

The electron beam to radiated energy conversion efficiency η can be calculated from $E_r = E_r^b + E_r^c$ and $B_\theta = B_\theta^b + B_\theta^c$, where Eq. (1) is employed for the beam and image charge fields. The average energy radiated per particle per unit time is conveniently approximated as [42] $\dot{\varepsilon}_\gamma = 2\alpha m_e c^2 \chi^2/3\tau_c[1+4.8(1+\chi)\ln(1+1.7\chi)+2.44\chi^2]^{2/3}$, where $\alpha = e^2/\hbar c$ is the fine-structure constant, $\tau_c = \hbar/m_e c^2$ is the Compton time, and $\chi \approx \gamma|E_r - B_\theta|/F_{\rm cr}$. Thus,

$$\eta = \frac{2\pi \int_{-\infty}^{+\infty} dt \int_{-\infty}^{0} dx \int_{0}^{+\infty} dr\, r\rho(x,r,t)\dot{\varepsilon}_\gamma[\chi(x,r,t)]}{\gamma m_e c^2 q N_e}. \tag{2}$$

In Eq. (2) we have assumed that all electrons have the same initial momentum and energy $\gamma m_e c^2$. Furthermore, we have neglected the change of γ during the beam-foil interaction. The triple integral in Eq. (2) can be carried out numerically.

Figure 2 shows the results of 3D PIC simulations of a cold electron beam colliding with one 0.5μm-thick aluminum foil. The electron beam has 2 nC charge, 10 GeV energy, and Gaussian spatial distribution with $\sigma_\parallel = 0.55\,\mu$m, $\sigma_\perp = 1.25\,\mu$m, and 9.2×10^{26} m^{-3} density. Figure 2(a) displays a snapshot of the electron beam density when the beam center has reached the front surface of the foil. Figures 2(b) and 2(c) show the transverse magnetic $\boldsymbol{B}_\perp$ and electric field $\boldsymbol{E}_\perp$, respectively. Whilst $\boldsymbol{B}_\perp$ is amplified and its peak value nearly doubles with respect to the beam self-field (3.1×10^4 T), $\boldsymbol{E}_\perp$ is suppressed and much smaller than the beam self-field (9.4×10^{12} V/m).

Figure 2(d) [Fig. 2(e)] plots η in electron beam-single foil collision with the same parameters as above but for $\sigma_\parallel = 0.55\,\mu$m ($\sigma_\perp = 0.55\,\mu$m) and $\sigma_\perp$ ($\sigma_\parallel$) ranging from $0.275\,\mu$m to $1.25\,\mu$m. Black circles and blue circles correspond to 3D PIC simulation and reflected model results, respectively. These simulations confirmed that the mechanism of beam focusing and photon emission is robust and effective in a range of parameters that could become within reach of existing accelerator facilities such as FACET II [51].

Figures 2(d)-(e) show that simulation results approach the prediction of the reflected field model with increasing (decreasing) $\sigma_\perp$ ($\sigma_\parallel$). For beam density smaller than the foil electron density, simulations indicate that foil thickness is irrelevant provided that collisions and plasma instabilities remain negligible. By contrast, foil thickness is important when the electron beam density exceeds the conductor density [43]. Note that synchrotron photon emission also occurs when the beam exits the foil, as

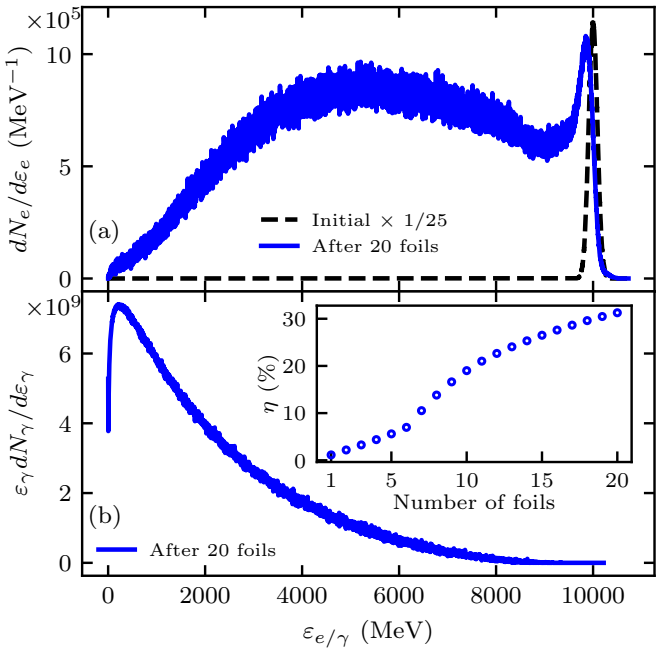

FIG. 4. (a) Initial (black dashed line) and final (blue line) electron beam energy distribution. (b) Final photon spectrum. The inset displays η as a function of the number of foils crossed by the electron beam.

E_r is suppressed at the rear foil surface and B_θ grows gradually during the beam exit [52]. However, for $\sigma_\perp \gtrsim \sigma_\parallel$, the rear surface contribution to the radiated energy is subdominant, and is neglected in our model.

The above considerations suggest that the effect can be substantially enhanced by colliding the self-focused beam with further foils. In fact, the increased beam density due to self-focusing results in stronger beam self-fields at the subsequent beam-foil collisions. Consequently, one expects that both self-focusing and photon emission should grow with increasing number of beam-foil collisions. This expectation is corroborated by our simulation results (see Figs. 3-4). Note that, for efficient self-focusing, the distance between two consecutive foils needs to be sufficiently large to allow beam self-field restoration around its propagation axis ($r \lesssim \sigma_\perp$). This requires that the travelled distance is much larger than $\sigma_\perp$. Furthermore, the interfoil distance needs to be short enough to prevent beam expansion. This can be estimated by considering the effect of $|\boldsymbol{f}_\perp| \approx |2qB_\theta|$ calculated at $x \approx x_0 + vt$ and $r \approx \sigma_\perp$, i.e., where focusing is stronger. For $\sigma_\perp \gtrsim \sigma_\parallel$, CTR extends approximately over a distance $\sigma_\perp^2/\sigma_\parallel$, which is larger than the beam length $\sigma_\parallel$. Thus, $|\boldsymbol{f}_\perp|$ lasts for approximately $\sigma_\parallel/c$, and the deflection angle is $\vartheta \approx |\boldsymbol{f}_\perp|\sigma_\parallel/\gamma m_e c^2$. Hence, to prevent defocusing the interfoil distance must be much smaller than $\sigma_\perp/\vartheta$.

In our multifoil 3D PIC simulations, the electron beam has 2 nC charge, Gaussian spatial and momentum distribution with $\sigma_\parallel = \sigma_\perp = 0.55\ \mu$m, 10 GeV mean energy, 212 MeV full width at half maximum (FWHM) energy spread, and 3 mm-mrad normalized emittance ($\vartheta \approx 2$ mrad with these parameters). The beam collides with 20 consecutive aluminum foils with $0.5\,\mu$m thickness, $10\,\mu$m interfoil distance, and 1.8×10^{29} m^{-3} initial electron density. The computational box size is $6.6\,\mu\text{m}(x) \times 8.8\,\mu\text{m}(y) \times 8.8\,\mu\text{m}(z)$ with $528(x) \times 352(y) \times 352(z)$ gridpoints, 4 particles-per-cell (ppc) for beam electrons and 8 ppc for foil electrons and ions were used. Simulations were independently performed with Smilei [53, 54] and CALDER [55] PIC codes with good agreement. The initial self-consistent beam fields, the effect of field and collisional ionization and binary Coulomb collisions were included. Synchrotron and bremsstrahlung emission, and multiphoton Breit-Wheeler and Bethe-Heitler pair production were implemented with state-of-the-art Monte-Carlo methods [43, 54, 56, 57]. Consistently with the submicrometer foil thickness, simulations showed that collisional processes are negligible.

Figure 3 displays snapshots of the electron and gamma beam evolution (see Supplemental Material for a movie). Until the 6$^{\text{th}}$ foil, the beam interacts with the field "reflected" by each foil. This leads to the self-focusing of the beam which gradually increases its density (see the first to third column of Fig. 3). The electron beam density rises from its initial value of 4.7×10^{27} m^{-3} to 8.2×10^{28} m^{-3} after the 6$^{\text{th}}$ foil, while the maximum photon density and χ are 2.9×10^{28} m^{-3} and 0.8, respectively [see Fig. 3(a3)-(d3)]. In the interaction with the 7$^{\text{th}}$ foil, the electron beam density reaches 3.8×10^{29} m^{-3}, which exceeds the foil density of 1.8×10^{29} m^{-3}. Hence, the foil is unable to reflect the fields of the beam, and a channel where foil electrons are expelled is created [see Fig. 3(b4)-(c4)]. Here χ and the photon beam density rise up to 3 and 4.1×10^{29} m^{-3}, respectively. Moreover, a fraction of approximately 10^{-4} photons with energies $> 2m_e c^2$ convert into $e^- e^+$ pairs via the multiphoton Breit-Wheeler process. Electron beam density stops increasing when it becomes larger than the foil electron density. In the following beam-foil collisions, the electron density beam profile undergoes longitudinal modulations [see Fig. 3(a5)-(a6)]. These modulations arise because the reflected field strength is dependent on the longitudinal position and stronger around the rear part of the beam, which yields a longitudinally inhomogeneous focusing force.

Figure 4(a) plots the initial (black dashed line) and final (blue line) electron beam energy distribution after the interaction with 20 consecutive foils. The broad distribution around approximately 5 GeV results from intense synchrotron emission occurring in the central and rear part of the electron beam. The residual peak around the initial electron beam energy is indicative of the small synchrotron and collisional energy losses of the front part of the beam, which experiences only weak amplitude CTR.

Figure 4(b) reports the final photon spectrum and the conversion efficiency η (inset) as a function of the number of crossed foils. The increase of η at the 7^{th} foil is due to the extremely high beam density and, consequently, to the ultrastrong fields induced inside the foil. After colliding with 20 foils, more than 30% of the electron beam energy is converted into a collimated (5 mrad rms photon energy angular distribution), 4 fs FWHM duration, 2.8×10^{29} m^{-3} peak density gamma-ray pulse.

In summary, we have introduced a new scheme to efficiently produce extremely dense gamma-ray beams from the interaction of a high-current ultrarelativistic electron beam with a sequence of thin foils. This scheme also provides a promising route to producing solid-density ultrarelativistic electron beams and to exploring strong-field QED processes with a single electron beam without the need of an external powerful laser drive.

Acknowledgments – This work was performed in the framework of the E-305 collaboration. E-305 is a SLAC experiment whose aims include the generation of bright gamma rays, in particular in electron beam-solid interaction. This article comprises parts of the PhD thesis work of Archana Sampath to be submitted to the Heidelberg University, Germany.

The work at LOA was supported by the European Research Council (ERC) under the European Unions Horizon 2020 research and innovation programme (Grant Agreement No. 715807). We acknowledge GENCI for granting us access to the supercomputer Irene under the grant No. A0080510786 to run CALDER simulations. The work at SLAC was supported by U.S. DOE FES grant No. FWP100331. UCLA was supported by U.S. Department of Energy grant DE-SC001006 and NSF grant 1734315.

* matteo.tamburini@mpi-hd.mpg.de

[1] Donald H Bilderback, Pascal Elleaume, and Edgar Weckert, "Review of third and next generation synchrotron light sources," J. Phys. B **38**, S773–S797 (2005).

[2] Joachim Ullrich, Artem Rudenko, and Robert Moshammer, "Free-Electron Lasers: New Avenues in Molecular Physics and Photochemistry," Annu. Rev. Phys. Chem. **63**, 635–660 (2012).

[3] S. Corde, K. Ta Phuoc, G. Lambert, R. Fitour, V. Malka, A. Rousse, A. Beck, and E. Lefebvre, "Femtosecond x rays from laser-plasma accelerators," Rev. Mod. Phys. **85**, 1–48 (2013).

[4] http://www.lightsources.org/.

[5] M. Gari and H. Hebach, "Photonuclear reactions at intermediate energies (40 MeV $\leq E_\gamma \leq$ 400 MeV)," Physics Reports **72**, 1–55 (1981).

[6] A. Di Piazza, C. Müller, K. Z. Hatsagortsyan, and C. H. Keitel, "Extremely high-intensity laser interactions with fundamental quantum systems," Rev. Mod. Phys. **84**, 1177–1228 (2012).

[7] "Extreme Light Infrastructure - Nuclear Physics facility (ELI-NP)," http://www.eli-np.ro/.

[8] "Deutsches Elektronen-Synchrotron (DESY)," http://photon-science.desy.de/facilities.

[9] C. P. Ridgers, C. S. Brady, R. Duclous, J. G. Kirk, K. Bennett, T. D. Arber, A. P. L. Robinson, and A. R. Bell, "Dense electron-positron plasmas and ultraintense γ rays from laser-irradiated solids," Phys. Rev. Lett. **108**, 165006 (2012).

[10] Tatsufumi Nakamura, James K. Koga, Timur Zh. Esirkepov, Masaki Kando, Georg Korn, and Sergei V. Bulanov, "High-power γ-ray flash generation in ultraintense laser-plasma interactions," Phys. Rev. Lett. **108**, 195001 (2012).

[11] L. L. Ji, A. Pukhov, E. N. Nerush, I. Yu. Kostyukov, B. F. Shen, and K. U. Akli, "Energy partition, γ-ray emission, and radiation reaction in the near-quantum electrodynamical regime of laser-plasma interaction," Phys. Plasmas **21**, 023109 (2014).

[12] Jian-Xing Li, Karen Z. Hatsagortsyan, Benjamin J. Galow, and Christoph H. Keitel, "Attosecond gamma-ray pulses via nonlinear compton scattering in the radiation-dominated regime," Phys. Rev. Lett. **115**, 204801 (2015).

[13] Xing-Long Zhu, Yan Yin, Tong-Pu Yu, Fu-Qiu Shao, Zhe-Yi Ge, Wei-Quan Wang, and Jin-Jin Liu, "Enhanced electron trapping and γ ray emission by ultra-intense laser irradiating a near-critical-density plasma filled gold cone," New Journal of Physics **17**, 053039 (2015).

[14] D. J. Stark, T. Toncian, and A. V. Arefiev, "Enhanced multi-mev photon emission by a laser-driven electron beam in a self-generated magnetic field," Phys. Rev. Lett. **116**, 185003 (2016).

[15] H. X. Chang, B. Qiao, T. W. Huang, Z. Xu, C. T. Zhou, Y. Q. Gu, X. Q. Yan, M. Zepf, and X. T. He, "Brilliant petawatt gamma-ray pulse generation in quantum electrodynamic laser-plasma interaction," Scientific Reports **7**, 45031 (2017).

[16] Wei-Min Wang, Zheng-Ming Sheng, Paul Gibbon, Li-Ming Chen, Yu-Tong Li, and Jie Zhang, "Collimated ultrabright gamma rays from electron wiggling along a petawatt laser-irradiated wire in the qed regime," Proceedings of the National Academy of Sciences **115**, 9911 (2018).

[17] T. W. Huang, C. M. Kim, C. T. Zhou, C. M. Ryu, K. Nakajima, S. C. Ruan, and C. H. Nam, "Table-top laser-driven gamma-ray source with nanostructured double-layer target," Plasma Physics and Controlled Fusion **60**, 115006 (2018).

[18] T. W. Huang, C. M. Kim, C. T. Zhou, M. H. Cho, K. Nakajima, C. M. Ryu, S. C. Ruan, and C. H. Nam, "Highly efficient laser-driven compton gamma-ray source," New Journal of Physics **21**, 013008 (2019).

[19] M. Vranic, T. Grismayer, S. Meuren, R. A. Fonseca, and L. O. Silva, "Are we ready to transfer optical light to gamma-rays?" Physics of Plasmas **26**, 053103 (2019).

[20] Martin Jirka, Ondrej Klimo, Yan-Jun Gu, and Stefan Weber, "Enhanced photon emission from a double-layer target at moderate laser intensities," Scientific Reports **10**, 8887 (2020).

[21] Xing-Long Zhu, Min Chen, Su-Ming Weng, Tong-Pu Yu, Wei-Min Wang, Feng He, Zheng-Ming Sheng, Paul McKenna, Dino A. Jaroszynski, and Jie Zhang, "Extremely brilliant gev γ-rays from a two-stage laser-plasma accelerator," Science Advances **6**, eaaz7240 (2020).

[22] Alberto Benedetti, Matteo Tamburini, and Christoph H. Keitel, "Giant collimated gamma-ray flashes," Nat. Photon. **12**, 319–323 (2018).

[23] M. Jirka, O. Klimo, S. V. Bulanov, T. Zh. Esirkepov, E. Gelfer, S. S. Bulanov, S. Weber, and G. Korn, "Electron dynamics and γ and e^-e^+ production by colliding laser pulses," Phys. Rev. E **93**, 023207 (2016).

[24] Matteo Tamburini, Antonino Di Piazza, and Christoph H. Keitel, "Laser-pulse-shape control of seeded qed cascades," Sci. Rep. **7**, 5694 (2017).

[25] A. Gonoskov, A. Bashinov, S. Bastrakov, E. Efimenko, A. Ilderton, A. Kim, M. Marklund, I. Meyerov, A. Muraviev, and A. Sergeev, "Ultrabright gev photon source via controlled electromagnetic cascades in laser-dipole waves," Phys. Rev. X **7**, 041003 (2017).

[26] J. Magnusson, A. Gonoskov, M. Marklund, T. Zh. Esirkepov, J. K. Koga, K. Kondo, M. Kando, S. V. Bulanov, G. Korn, and S. S. Bulanov, "Laser-particle collider for multi-gev photon production," Phys. Rev. Lett. **122**, 254801 (2019).

[27] V. Yakimenko, S. Meuren, F. Del Gaudio, C. Baumann, A. Fedotov, F. Fiuza, T. Grismayer, M. J. Hogan, A. Pukhov, L. O. Silva, and G. White, "Prospect of studying nonperturbative QED with beam-beam collisions," Phys. Rev. Lett. **122**, 190404 (2019).

[28] F. Del Gaudio, T. Grismayer, R. A. Fonseca, W. B. Mori, and L. O. Silva, "Bright γ rays source and nonlinear breit-wheeler pairs in the collision of high density particle beams," Phys. Rev. Accel. Beams **22**, 023402 (2019).

[29] Matteo Tamburini and Sebastian Meuren, "Efficient High-Energy Photon Production in the Supercritical QED Regime," arXiv e-prints , arXiv:1912.07508 (2019).

[30] H.-P. Schlenvoigt, K. Haupt, A. Debus, F. Budde, O. Jäckel, S. Pfotenhauer, H. Schwoerer, E. Rohwer, J. G. Gallacher, E. Brunetti, R. P. Shanks, S. M. Wiggins, and D. A. Jaroszynski, "A compact synchrotron radiation source driven by a laser-plasma wakefield accelerator," Nature Physics **4**, 130–133 (2008).

[31] S. Kneip, C. McGuffey, J. L. Martins, S. F. Martins, C. Bellei, V. Chvykov, F. Dollar, R. Fonseca, C. Huntington, G. Kalintchenko, A. Maksimchuk, S. P. D. Mangles, T. Matsuoka, S. R. Nagel, C. A. J. Palmer, J. Schreiber, K. Ta Phuoc, A. G. R. Thomas, V. Yanovsky, L. O. Silva, K. Krushelnick, and Z. Najmudin, "Bright spatially coherent synchrotron x-rays from a table-top source," Nature Physics **6**, 980–983 (2010).

[32] Silvia Cipiccia, Mohammad R. Islam, Bernhard Ersfeld, Richard P. Shanks, Enrico Brunetti, Gregory Vieux, Xue Yang, Riju C. Issac, Samuel M. Wiggins, Gregor H. Welsh, Maria-Pia Anania, Dzmitry Maneuski, Rachel Montgomery, Gary Smith, Matthias Hoek, David J. Hamilton, Nuno R. C. Lemos, Dan Symes, Pattathil P. Rajeev, Val O. Shea, Joao M. Dias, and Dino A. Jaroszynski, "Gamma-rays from harmonically resonant betatron oscillations in a plasma wake," Nat. Phys. **7**, 867–871 (2011).

[33] K. Ta Phuoc, S. Corde, C. Thaury, V. Malka, A. Tafzi, J. P. Goddet, R. C. Shah, S. Sebban, and A. Rousse, "All-optical Compton gamma-ray source," Nat. Photon. **6**, 308–311 (2012).

[34] G. Sarri, D. J. Corvan, W. Schumaker, J. M. Cole, A. Di Piazza, H. Ahmed, C. Harvey, C. H. Keitel, K. Krushelnick, S. P. D. Mangles, Z. Najmudin, D. Symes, A. G. R. Thomas, M. Yeung, Z. Zhao, and M. Zepf, "Ultrahigh Brilliance Multi-MeV γ-Ray Beams from Nonlinear Relativistic Thomson Scattering," Phys. Rev. Lett. **113**, 224801 (2014).

[35] Wenchao Yan, Colton Fruhling, Grigory Golovin, Daniel Haden, Ji Luo, Ping Zhang, Baozhen Zhao, Jun Zhang, Cheng Liu, Min Chen, Shouyuan Chen, Sudeep Banerjee, and Donald Umstadter, "High-order multiphoton thomson scattering," Nature Photonics **11**, 514–520 (2017).

[36] J. M. Cole, K. T. Behm, E. Gerstmayr, T. G. Blackburn, J. C. Wood, C. D. Baird, M. J. Duff, C. Harvey, A. Ilderton, A. S. Joglekar, K. Krushelnick, S. Kuschel, M. Marklund, P. McKenna, C. D. Murphy, K. Poder, C. P. Ridgers, G. M. Samarin, G. Sarri, D. R. Symes, A. G. R. Thomas, J. Warwick, M. Zepf, Z. Najmudin, and S. P. D. Mangles, "Experimental evidence of radiation reaction in the collision of a high-intensity laser pulse with a laser-wakefield accelerated electron beam," Phys. Rev. X **8**, 011020 (2018).

[37] K. Poder, M. Tamburini, G. Sarri, A. Di Piazza, S. Kuschel, C. D. Baird, K. Behm, S. Bohlen, J. M. Cole, D. J. Corvan, M. Duff, E. Gerstmayr, C. H. Keitel, K. Krushelnick, S. P. D. Mangles, P. McKenna, C. D. Murphy, Z. Najmudin, C. P. Ridgers, G. M. Samarin, D. R. Symes, A. G. R. Thomas, J. Warwick, and M. Zepf, "Experimental signatures of the quantum nature of radiation reaction in the field of an ultraintense laser," Phys. Rev. X **8**, 031004 (2018).

[38] Gerard A. Mourou, Toshiki Tajima, and Sergei V. Bulanov, "Optics in the relativistic regime," Rev. Mod. Phys. **78**, 309–371 (2006).

[39] Mattias Marklund and Padma K. Shukla, "Nonlinear collective effects in photon-photon and photon-plasma interactions," Rev. Mod. Phys. **78**, 591–640 (2006).

[40] Remo Ruffini, Gregory Vereshchagin, and She-Sheng Xue, "Electron-positron pairs in physics and astrophysics: From heavy nuclei to black holes," Physics Reports **487**, 1–140 (2010).

[41] V. I. Ritus, "Quantum effects of the interaction of elementary particles with an intense electromagnetic field," J. Russ. Laser Res. **6**, 497–617 (1985).

[42] V. N. Baier, V. M. Katkov, and V. M. Strakhovenko, *Electromagnetic Processes at High Energies in Oriented Single Crystals* (World Scientific, Singapore, 1998).

[43] Archana Sampath, "Ph.D. thesis, Ruprecht-Karls-Universität, Heidelberg," (to be submitted).

[44] J. D. Jackson, *Classical Electrodynamics*, 3rd ed. (John Wiley and Sons, Inc., 1998).

[45] P. Hammond, "Electric and magnetic images," Proceedings of the IEE - Part C: Monographs **107**, 306–313 (1960).

[46] R. J. Adler, "Image-field focusing of intense ultrarelativistic electron beams in vacuum," Part. Accel. **12**, 39–44 (1982).

[47] S. Humphries, "Equilibria for foil-focused relativistic electron beams," Part. Accel. **13**, 249–253 (1983).

[48] S. Humphries and Carl B. Ekdahl, "Image charge focusing of relativistic electron beams," Journal of Applied Physics **63**, 583–585 (1988).

[49] S. Humphries, Carl Ekdahl, and D. M. Woodall, "Image current guiding of a relativistic electron beam in a foil focusing system," Appl. Phys. Lett. **54**, 2195–2197 (1989).

[50] R. F. Fernsler, R. F. Hubbard, and S. P. Slinker, "Foil focusing of electron beams," J. Appl. Phys. **68**, 5985–

5994 (1990).
[51] V. Yakimenko, L. Alsberg, E. Bong, G. Bouchard, C. Clarke, C. Emma, S. Green, C. Hast, M. J. Hogan, J. Seabury, N. Lipkowitz, B. O'Shea, D. Storey, G. White, and G. Yocky, "FACET-II facility for advanced accelerator experimental tests," Phys. Rev. Accel. Beams **22**, 101301 (2019).
[52] N. J. Carron, "Fields of particles and beams exiting a conductor," Progress In Electromagnetics Research **28**, 147–183 (2000).
[53] J. Derouillat, A. Beck, F. Prez, T. Vinci, M. Chiaramello, A. Grassi, M. Fl, G. Bouchard, I. Plotnikov, N. Aunai, J. Dargent, C. Riconda, and M. Grech, "Smilei : A collaborative, open-source, multi-purpose particle-in-cell code for plasma simulation," Computer Physics Communications **222**, 351 – 373 (2018).
[54] "Smilei particle-in-cell code," `https://smileipic.github.io/Smilei/`.
[55] E. Lefebvre, N. Cochet, S. Fritzler, V. Malka, M.-M. Aléonard, J.-F. Chemin, S. Darbon, L. Disdier, J. Faure, A. Fedotoff, O. Landoas, G. Malka, V. Méot, P. Morel, M. Rabec Le Gloahec, A. Rouyer, Ch Rubbelynck, V. Tikhonchuk, R. Wrobel, P. Audebert, and C. Rousseaux, "Electron and photon production from relativistic laser-plasma interactions," Nuclear Fusion **43**, 629–633 (2003).
[56] M. Lobet, E. d'Humières, M. Grech, C. Ruyer, X. Davoine, and L. Gremillet, "Modeling of radiative and quantum electrodynamics effects in pic simulations of ultra-relativistic laser-plasma interaction," Journal of Physics: Conference Series **688**, 012058 (2016).
[57] B. Martinez, M. Lobet, R. Duclous, E. d'Humières, and L. Gremillet, "High-energy radiation and pair production by coulomb processes in particle-in-cell simulations," Physics of Plasmas **26**, 103109 (2019).

Supplemental Material for "Extremely Dense Gamma-Ray Pulses in Electron Beam-Multifoil Collisions"

Archana Sampath,[1] Xavier Davoine,[2,3] Sébastien Corde,[4] Laurent Gremillet,[2,3] Maitreyi Sangal,[1] Christoph H. Keitel,[1] Robert Ariniello,[5] John Cary,[5] Henrik Ekerfelt,[6] Claudio Emma,[6] Frederico Fiuza,[6] Hiroki Fujii,[7] Max Gilljohann,[4] Mark Hogan,[6] Chan Joshi,[7] Alexander Knetsch,[4] Olena Kononenko,[4] Valentina Lee,[5] Mike Litos,[5] Kenneth Marsh,[7] Zan Nie,[7] Brendan O'Shea,[6] J. Ryan Peterson,[6,8] Pablo San Miguel Claveria,[4] Doug Storey,[6] Yipeng Wu,[7] Xinlu Xu,[6] Chaojie Zhang,[7] and Matteo Tamburini[1,*]

[1] *Max-Planck-Institut für Kernphysik, Saupfercheckweg 1, D-69117 Heidelberg, Germany*
[2] *CEA, DAM, DIF, 91297 Arpajon, France*
[3] *Université Paris-Saclay, CEA, LMCE, 91680 Bruyères-le-Châtel, France*
[4] *LOA, ENSTA Paris, CNRS, Ecole Polytechnique, Institut Polytechnique de Paris, 91762 Palaiseau, France*
[5] *University of Colorado Boulder, Department of Physics, Center for Integrated Plasma Studies, Boulder, Colorado 80309, USA*
[6] *SLAC National Accelerator Laboratory, Menlo Park, CA 94025, USA*
[7] *University of California Los Angeles, Los Angeles, CA 90095, USA*
[8] *Stanford University, Physics Department, Stanford, CA 94305, USA*

(Dated: September 25, 2020)

S1. TRANSITION RADIATION BY AN ULTRARELATIVISTIC PARTICLE BEAM IN THE NEAR-FIELD ZONE

A. Pseudophoton method

Let us consider an ultrarelativistic particle beam with cylindrical symmetry around its propagation axis and moving along $x > 0$ at a velocity v in the laboratory frame. In its rest frame, the beam density distribution is chosen as

$$n'(\mathbf{x}') = n'_0 e^{-r'^2/2\sigma'^2_\perp - x'^2/2\sigma'^2_\parallel} \,. \tag{S1}$$

Here primed quantities refer to their values in the beam rest frame, $n'_0 = N_e/(2\pi)^{3/2}\sigma'^2_\perp\sigma'_\parallel$, and N_e is the number of beam particles of individual charge q. We assume that the longitudinal and transverse (rms) beam dimensions fulfill $\sigma'_\parallel = \gamma\sigma_\parallel \gg \sigma'_\perp = \sigma_\perp$, where $\gamma = (1 - v^2/c^2)^{-1/2}$ is the beam relativistic factor. Hence, the beam self-electric field can be evaluated from Gauss' law in the long-beam limit

$$\mathbf{E}'^b(\mathbf{x}') \approx \mathbf{E}^b_\perp(\mathbf{x}') \approx 4\pi n'_0 q\sigma'^2_\perp \frac{\left(1 - e^{-r'^2/2\sigma'^2_\perp}\right)}{r} e^{-x'^2/2\sigma'^2_\parallel}\,\hat{\mathbf{r}}\,, \tag{S2}$$

which is valid for $r' \ll \sigma'_\parallel$, i.e., $r \ll \gamma\sigma_\parallel$. An inverse Lorentz transformation yields the beam self-field in the laboratory frame

$$\mathbf{E}^b_\perp(x, r, t) \approx 4\pi n_0 q\sigma^2_\perp \frac{\left(1 - e^{-r^2/2\sigma^2_\perp}\right)}{r} e^{-(x-vt)^2/2\sigma^2_\parallel}\,\hat{\mathbf{r}}\,. \tag{S3}$$

Here we have introduced the beam density in the laboratory $n_0 = \gamma n'_0$ and, for simplicity, the time origin is chosen such that at $t = 0$ the beam center is located at $x = 0$.

By using the Weizsäcker-Williams approximation [1] the beam electric self-field can be decomposed into plane waves (pseudophotons) whose electric components are

$$\widetilde{\mathbf{E}}^b_\perp(x, \mathbf{k}_\perp, \omega) = \iint d^2\mathbf{r}_\perp dt\, \mathbf{E}^b_\perp(x, r, t) e^{-i\mathbf{k}_\perp\cdot\mathbf{r}_\perp + i\omega t} = -8i\sqrt{2}\pi^{5/2} n_0 q \frac{\sigma_\parallel\sigma^2_\perp}{k_\perp v} e^{i\omega x/v} e^{-\sigma^2_\parallel\omega^2/2v^2 - \sigma^2_\perp k^2_\perp/2}\,\widehat{\mathbf{k}}_\perp\,, \tag{S4}$$

* matteo.tamburini@mpi-hd.mpg.de

where we have used the integral formulae [2]

$$\int_0^{2\pi} d\phi\, \cos\phi e^{ik_\perp r\cos\phi} = 2i\pi\, J_1(k_\perp r)\,, \tag{S5}$$

$$\int_0^{\infty} dr\, J_\nu(k_\perp r) = 1/k_\perp\,, \tag{S6}$$

$$\int_0^{\infty} dr e^{-r^2/2\sigma_\perp^2}\, J_1(k_\perp r) = \sqrt{\frac{\pi}{2}}\sigma_\perp e^{-\sigma_\perp^2 k_\perp^2/4} I_{1/2}\left(\sigma_\perp^2 k_\perp^2/4\right)\,, \tag{S7}$$

with $I_{1/2}(z) = \sqrt{2/\pi}\sinh(z)/\sqrt{z}$.

In the case of a perfect conductor with front surface at $x = 0$, the sum of the transverse incident ($\widetilde{\mathbf{E}}_\perp^b$) and induced/scattered conductor ($\widetilde{\mathbf{E}}_\perp^c$) electric fields should vanish at the boundary, so that

$$\widetilde{\mathbf{E}}_\perp^c(0^-, \mathbf{k}_\perp, \omega) = -\widetilde{\mathbf{E}}_\perp^b(0^-, \mathbf{k}_\perp, \omega)\,. \tag{S8}$$

The scattered field can then be exactly computed at any time and position in vacuum ($x < 0$) by using the plane-wave decomposition [3]

$$\begin{aligned}\mathbf{E}_\perp^c(x, \mathbf{r}_\perp, t) &= (2\pi)^{-3}\iint d\omega d^2\mathbf{k}_\perp\, \widetilde{\mathbf{E}}_\perp^c(0^-, \mathbf{k}_\perp, \omega)\, e^{-i\omega t + ik_x x + i\mathbf{k}_\perp\cdot\mathbf{r}_\perp} \\ &= i\sqrt{\frac{2}{\pi}}\frac{n_0 q}{v}\sigma_\parallel\sigma_\perp^2 \int_{-\infty}^{\infty} d\omega\, e^{-\sigma_\parallel^2\omega^2/2v^2 - i\omega t}\int \frac{d^2\mathbf{k}_\perp}{k_\perp}\, e^{-\sigma_\perp^2 k_\perp^2/2 + i\mathbf{k}_\perp\cdot\mathbf{r}_\perp + ik_x x}\,\widehat{\mathbf{k}}_\perp\,.\end{aligned} \tag{S9}$$

We have introduced the longitudinal wavenumber

$$k_x = \begin{cases} -\mathrm{sgn}(\omega)\sqrt{\omega^2/c^2 - k_\perp^2} & \text{if } \omega^2/c^2 > k_\perp^2 \\ -i\sqrt{k_\perp^2 - \omega^2/c^2} & \text{if } \omega^2/c^2 < k_\perp^2 \end{cases} \tag{S10}$$

In Eq. (S9), Fourier components with $\omega^2/c^2 > k_\perp^2$ describe propagating waves, while components with $\omega^2/c^2 < k_\perp^2$ correspond to evanescent waves confined to the conductor's boundary [4]. The choice of the minus sign in the definition of k_x is consistent with waves propagating/damped along $x < 0$.

Equation (S9) can be simplified by expressing the transverse wavenumber as $\mathbf{k}_\perp = k_\perp(\cos\phi\,\widehat{\mathbf{r}} + \sin\phi\,\widehat{\boldsymbol{\phi}})$ and performing the integration over ϕ, which gives

$$\mathbf{E}_\perp^c(x, r, t) = E_r^c(x, r, t)\,\widehat{\mathbf{r}} = -\sqrt{8\pi}\frac{n_0 q}{v}\sigma_\parallel\sigma_\perp^2\int_{-\infty}^{\infty} d\omega\, e^{-\sigma_\parallel^2\omega^2/2v^2 - i\omega t}\int_0^{\infty} dk_\perp\, e^{-\sigma_\perp^2 k_\perp^2/2 + ik_x x} J_1(k_\perp r)\,\widehat{\mathbf{r}}\,. \tag{S11}$$

This equation is accurate in the domain of validity of the field approximation in Eq. (S3), and therefore holds in the near beam region that is of central interest here.

The longitudinal electric field follows from Gauss' law in vacuum [5],

$$\frac{\partial E_x^c}{\partial x} = -\frac{1}{r}\frac{\partial}{\partial r}\left(rE_r^c\right)\,, \tag{S12}$$

yielding

$$E_x^c(x, r, t) = -i\sqrt{8\pi}\frac{n_0 q}{v}\sigma_\parallel\sigma_\perp^2\int_{-\infty}^{\infty} d\omega\, e^{-\sigma_\parallel^2\omega^2/2v^2 - i\omega t}\int_0^{\infty} dk_\perp \frac{k_\perp}{k_x} e^{-\sigma_\perp^2 k_\perp^2/2 + ik_x x} J_0(k_\perp r)\,. \tag{S13}$$

Finally, the induced magnetic field is given by Faraday's law

$$\frac{1}{c}\frac{\partial B_\theta^c}{\partial t} = \frac{\partial E_x^c}{\partial r} - \frac{\partial E_r^c}{\partial x}\,, \tag{S14}$$

and by using Eq. (S10) one obtains

$$B_\theta^c(x, r, t) = -\sqrt{8\pi}\frac{n_0 q}{vc}\sigma_\parallel\sigma_\perp^2\int_{-\infty}^{\infty} d\omega\,\omega e^{-\sigma_\parallel^2\omega^2/2v^2 - i\omega t}\int_0^{\infty}\frac{dk_\perp}{k_x} e^{-\sigma_\perp^2 k_\perp^2/2 + ik_x x} J_1(k_\perp r)\,. \tag{S15}$$

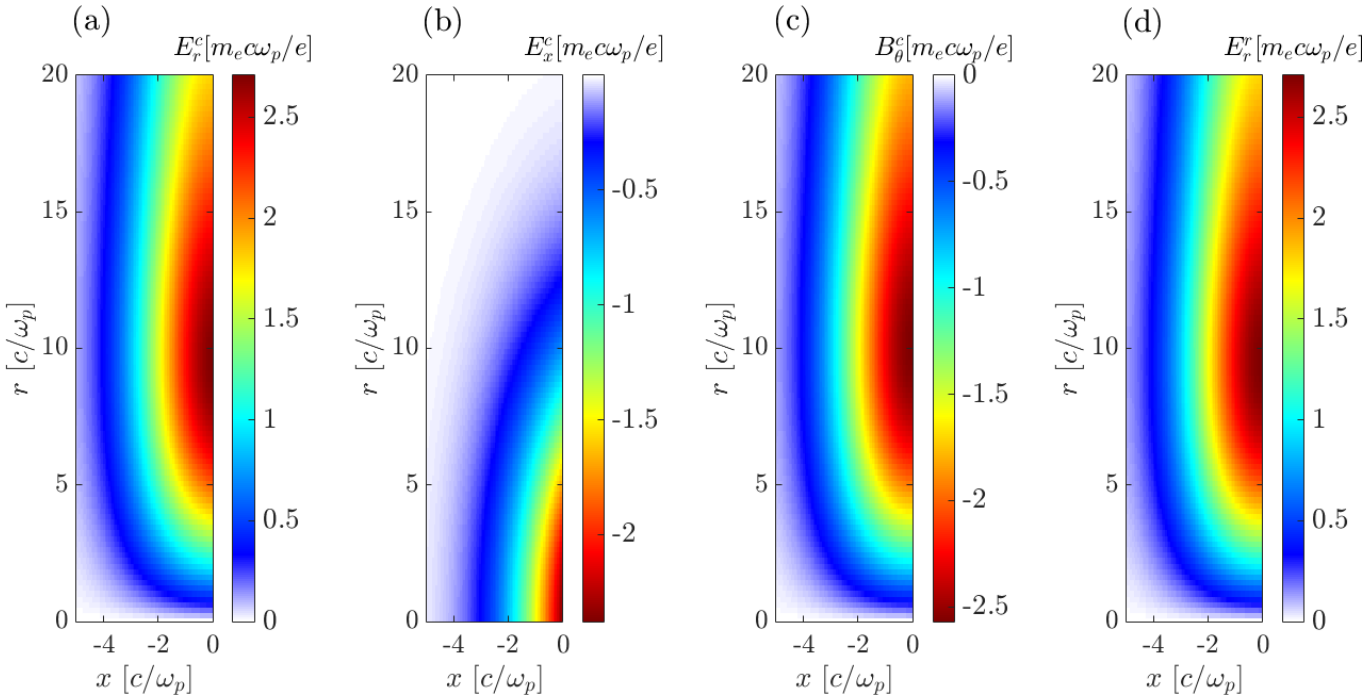

FIG. S1. (a) Transverse and (b) longitudinal electric and (c) magnetic field of the conductor, compared with (d) transverse electric field of the beam's image charge at $\omega_p t = 0$. Beam parameters are $\gamma = 2 \times 10^4$, $\sigma_\parallel \omega_p/c = 2$ and $\sigma_\perp \omega_p/c = 6$.

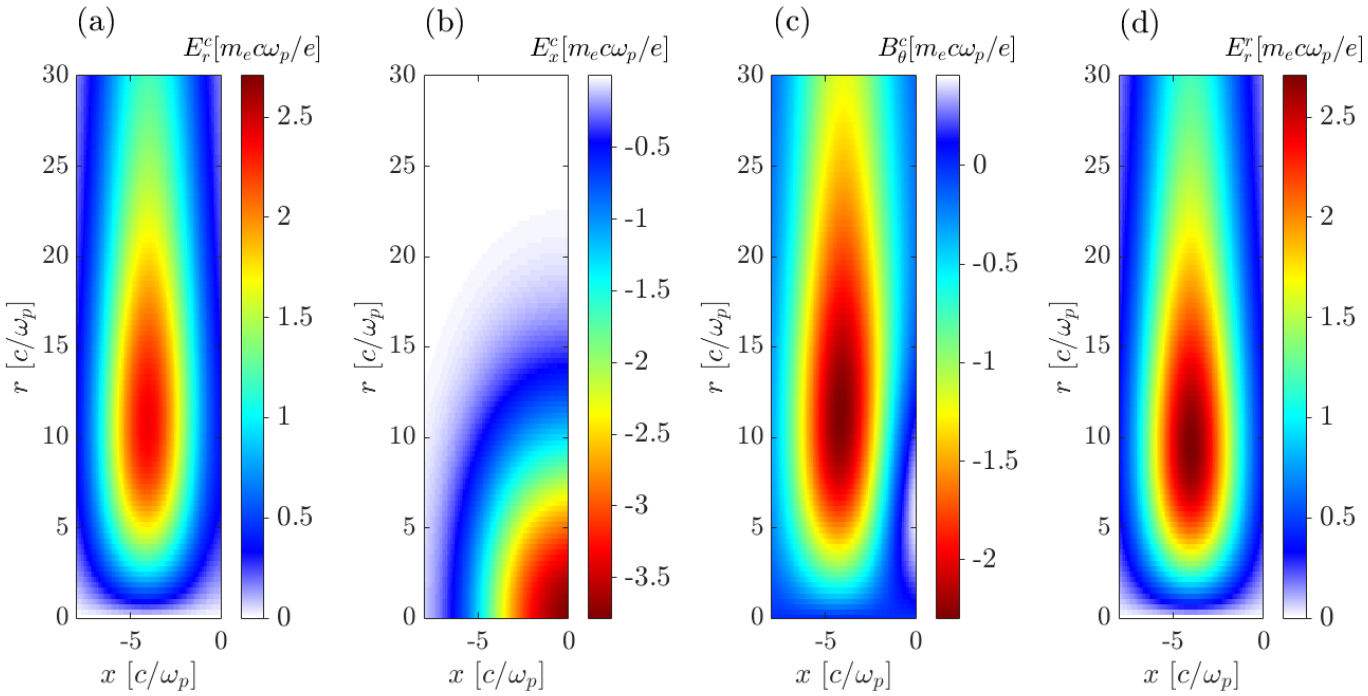

FIG. S2. Same as Fig. S1 but at a later time, $\omega_p t = 4$.

Figures S1 and S2 display 2D maps of the conductor electric (a)-(b) and magnetic (c) fields as computed numerically from Eqs. (S11), (S13), and (S15). We first consider an ultrarelativistic electron ($q = -e$) beam with $\gamma = 2 \times 10^4$, $\sigma_\parallel \omega_p/c = 2$ and $\sigma_\perp \omega_p/c = 6$, where $\omega_p = \sqrt{4\pi n_0 e^2/m_e}$ is the beam plasma frequency. These fields are compared with the radial electric field of the beam's image charge E_r^r (d) (the "reflected field"), obtained by setting $q \to -q$ and $v \to -v$ in Eq. (S3). At $t = 0$ (see Fig. S1), both the transverse conductor electric and magnetic fields E_r^c

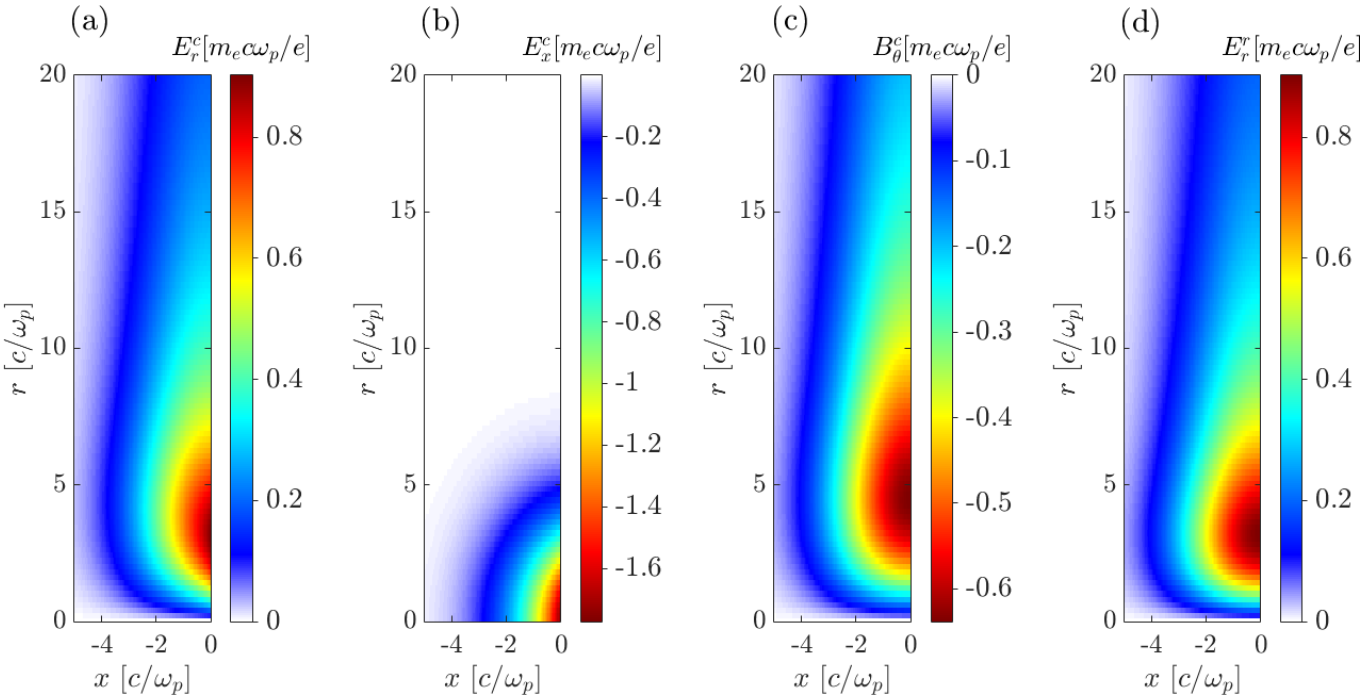

FIG. S3. (a) Transverse and (b) longitudinal electric and (c) magnetic field of the conductor, compared with (d) transverse electric field of the beam's image charge at $\omega_p t = 0$. Beam parameters are $\gamma = 2 \times 10^4$, $\sigma_\parallel \omega_p/c = 2$ and $\sigma_\perp \omega_p/c = 2$.

and B_θ^c are very similar to the reflected field around the boundary ($E_r^c \approx -B_\theta^c \approx E_r^r \approx 2.7\, m_e c\omega_p/e$). The induced longitudinal electric field has a maximum amplitude slightly lower ($E_x^c \approx -2.4\, m_e c\omega_p/e$), reached at $r = 0$ (in contrast to the transverse fields which peak at $r \approx 1.6\sigma_\perp \approx 9.5 c\omega_p$). At $\omega_p t = 4$ (see Fig. S2), the transverse induced fields detach from the boundary as is consistent for a propagating wavepacket. Yet diffraction causes these radiated fields to drop in amplitude ($E_r^c \approx 2.4\, m_e c\omega_p/e$ and $B_\theta^c \approx -2.3\, m_e c\omega_p/e$), and to reach their maxima at a larger radius ($r\omega_p/c \approx 11$) than the reflected field. The longitudinal induced field remains mainly confined to the boundary and has been intensified ($E_x^c \approx -3.8\, m_e c\omega_p/e$). Around the boundary and $r \approx \sigma_\perp$, the magnetic field is then mainly driven through $\partial B_\theta^c/c\partial t \approx \partial E_x^c/\partial r > 0$, and so becomes of positive polarity [see Fig. S2(c)]

Figures S3(a)-(d) plot the same quantities as Figs. S1-S2 but for a spherical beam ($\sigma_\parallel = \sigma_\perp = 2c/\omega_p$) and at $t = 0$. The scattered fields show a substantial divergence because the dominant wavenumber $\lambda \sim \sigma_\parallel$ is close to the transverse beam size $\sigma_\perp$. This translates into a longitudinal electric field E_x^c about twice stronger than E_r^c. The amplitude of the scattered magnetic field is close to, yet a bit lower than the beam self-field ($B_\theta^c \approx -0.64\, m_e c\omega_p/e$ vs. $B_\theta^b \approx 0.90\, m_e c\omega_p/e$).

The case of a longitudinally elongated beam ($\sigma_\parallel \omega_p/c = 6$, $\sigma_\perp \omega_p/c = 1$) is illustrated at two successive times in Figs. S4 and S5. The small $\sigma_\perp/\sigma_\parallel$ ratio leads to most of the induced fields being evanescent, and thus strongly localized at the conductor's boundary. At both $t = 0$ (see Fig. S4) and $\omega_p t = 5$ (see Fig. S5), the longitudinal electric field exceeds its transverse counterpart. In parallel, the induced magnetic field gets considerably weaker than the magnetic self-field of the beam, and changes polarity along the boundary [see Fig. S5(c)].

B. Evaluation of the surface magnetic field in the radiating and nonradiating regimes

We now demonstrate that the magnetic field induced at the boundary equals the beam self-field when $\sigma_\perp \gg \sigma_\parallel$ and tends to vanish when $\sigma_\perp \ll \sigma_\parallel$. To this purpose, we start by the expression of B_θ^c at $x = 0^-$

$$B_\theta^c(0^-, r, t) = -\sqrt{8\pi}\frac{n_0 q}{vc}\sigma_\parallel \sigma_\perp^2 \int_{-\infty}^{\infty} d\omega\, \omega e^{-\sigma_\parallel^2 \omega^2/2v^2 - i\omega t} \int_0^\infty \frac{dk_\perp}{k_x}\, e^{-\sigma_\perp^2 k_\perp^2/2} J_1(k_\perp r)\,. \tag{S16}$$

When $\sigma_\perp \gg \sigma_\parallel$, the dominant integration range over $k_\perp$ is such that $k_\perp^2 \ll \omega^2/c^2 \approx 2/\sigma_\parallel^2$, so that the scattered

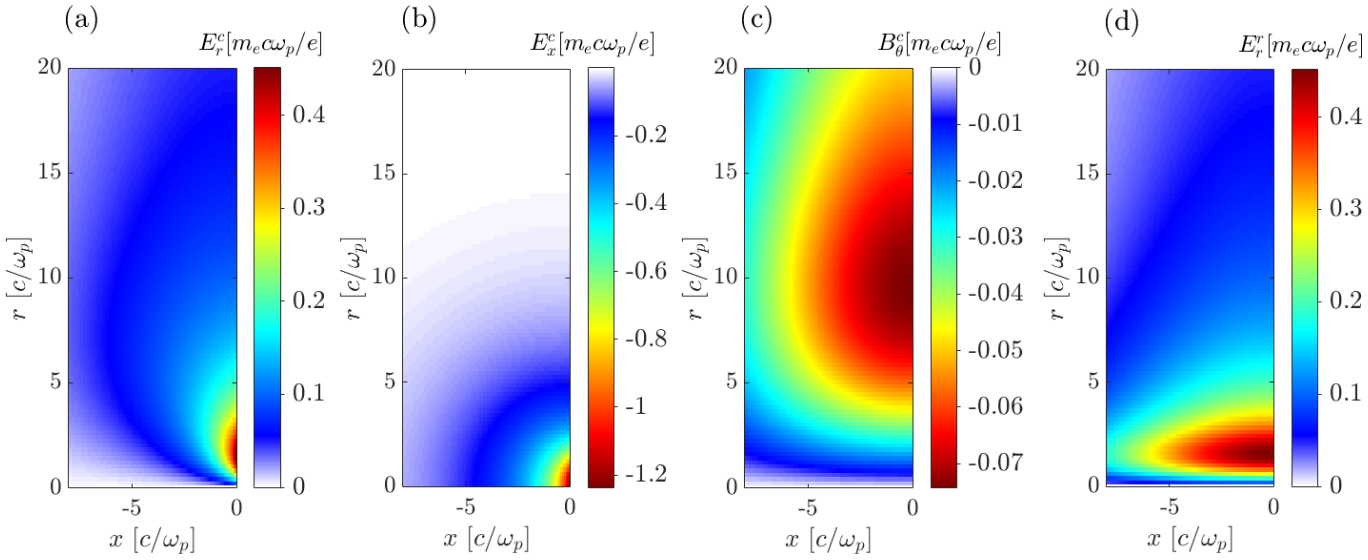

FIG. S4. (a) Transverse and (b) longitudinal electric and (c) magnetic field of the conductor, compared with (d) transverse electric field of the beam's image charge at $\omega_p t = 0$. Beam parameters are $\gamma = 2 \times 10^4$, $\sigma_\parallel \omega_p/c = 6$ and $\sigma_\perp \omega_p/c = 1$.

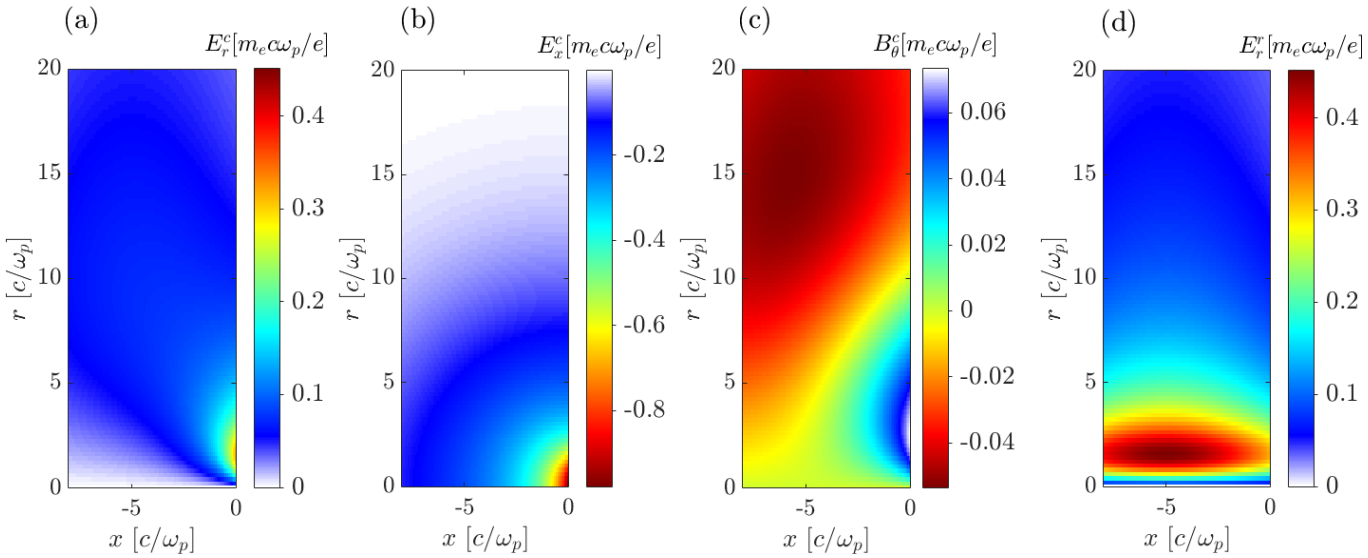

FIG. S5. Same as Fig. S4 but at a later time, $\omega_p t = 5$.

field mainly consists of propagating waves. Approximating $k_x \approx -\omega/c$ yields

$$B_\theta^c(0^-, r, t) \approx \sqrt{8\pi} \frac{n_0 q}{v} \sigma_\parallel \sigma_\perp^2 \int_{-\infty}^{\infty} d\omega\, e^{-\sigma_\parallel^2 \omega^2/2v^2 - i\omega t} \int_0^{\infty} dk_\perp\, e^{-\sigma_\perp^2 k_\perp^2/2} J_1(k_\perp r)\,. \tag{S17}$$

It is easily seen that the above approximate expression of $B_\theta^c(0^-, r, t)$ exactly coincides with $-E_r^c(0^-, r, t)$ from Eq. (S11). Since by construction $E_r^c(0^-, r, t) = -E_r^b(0^-, r, t) = -B_\theta^b(0^-, r, t)$, we conclude that $B_\theta^c(0^-, r, t) = B_\theta^b(0^-, r, t)$ in the radiating regime.

The calculation is more involved when $\sigma_\perp \ll \sigma_\parallel$. By using Eq. (S10), we first decompose the integral over $k_\perp$ in Eq. (S16) as

$$\begin{aligned}\int_0^{\infty} \frac{dk_\perp}{k_x} e^{-\sigma_\perp^2 k_\perp^2/2} J_1(k_\perp r) = -\mathrm{sgn}(\omega) \int_0^{|\omega|/c} dk_\perp \frac{J_1(k_\perp r)}{\sqrt{\omega^2/c^2 - k_\perp^2}} e^{-\sigma_\perp^2 k_\perp^2/2} \\ + i \int_{|\omega|/c}^{\infty} dk_\perp \frac{J_1(k_\perp r)}{\sqrt{k_\perp^2 - \omega^2/c^2}} e^{-\sigma_\perp^2 k_\perp^2/2} \equiv \mathcal{I}_1 + \mathcal{I}_2\,.\end{aligned} \tag{S18}$$

where the integrals $\mathcal{I}_1$ and $\mathcal{I}_2$ account for the propagating and non-propagating (evanescent) modes, respectively. In $\mathcal{I}_1$, one can neglect the variation of the exponential term because $\sigma_\perp k_\perp \leq \sigma_\perp \omega/c \sim (\sigma_\perp/\sigma_x) \ll 1$, and thus approximate this integral as

$$\mathcal{I}_1 \approx -\mathrm{sgn}(\omega)\int_0^{|\omega|/c} dk_\perp \frac{J_1(k_\perp r)}{\sqrt{\omega^2/c^2-k_\perp^2}} = -\mathrm{sgn}(\omega)\int_0^1 du \frac{J_1(|\omega| r u/c)}{\sqrt{1-u^2}} = -\frac{\sin^2(\omega r/2c)}{(\omega r/2c)}\,. \tag{S19}$$

The latter equality follows from Eq. 6.552-7 in [2], and by noting that $\sin^2(|\omega|r/2c) = \sin^2(\omega r/2c)$, and $\omega = \mathrm{sgn}(\omega)|\omega|$. To evaluate $\mathcal{I}_2$, we first recast it as

$$\mathcal{I}_2 = i\int_1^\infty du \frac{J_1(|\omega| r u/c)}{\sqrt{u^2-1}} e^{-\sigma_\perp^2\omega^2u^2/2c^2}\,. \tag{S20}$$

Let us first consider radial positions $r \ll \sigma_\perp$. In this case, the effective integration range is $[1, \sim \sqrt{2}c/\sigma_\perp|\omega|]$, and one can expand the Bessel function around zero $J_1(x) \approx x/2 + \mathcal{O}(x^3)$. This yields

$$\mathcal{I}_2 \approx i\frac{|\omega| r}{2c}\int_1^\infty du \frac{u\, e^{-(\sigma_\perp\omega u/c)^2/2}}{\sqrt{u^2-1}} = i\frac{|\omega| r}{4c}\int_1^\infty dw \frac{e^{-(\sigma_\perp\omega/c)^2 w/2}}{\sqrt{w-1}} = i\sqrt{\frac{\pi}{8}}\frac{r}{\sigma_\perp} e^{-(\sigma_\perp\omega/c)^2/2}\,. \tag{S21}$$

By plugging Eqs. (S19) and (S21) into Eq. (S16) and using $e^{-i\omega t} = \cos(\omega t) + (i/\omega) d\cos(\omega t)/dt$ one obtains

$$\begin{aligned} B_\theta^c(0^-, r\ll\sigma_\perp, t) \approx \sqrt{8\pi}\frac{n_0 q}{vc}\sigma_\parallel\sigma_\perp^2 \Bigg[&\frac{2c}{r}\int_{-\infty}^\infty d\omega\, e^{-(\sigma_\parallel\omega/v)^2/2}\sin^2(\omega r/2c)\cos(\omega t) \\ &+\sqrt{\frac{\pi}{8}}\frac{r}{\sigma_\perp}\frac{d}{dt}\int_{-\infty}^\infty d\omega\, e^{-(\sigma_\parallel^2/v^2+\sigma_\perp^2/c^2)\omega^2/2}\cos(\omega t)\Bigg]\,. \end{aligned} \tag{S22}$$

After some calculations, one obtains

$$\begin{aligned} B_\theta^c(0^-, r\ll\sigma_\perp, t) \approx 2\pi n_0 q r\Bigg[&\left(\frac{\sigma_\perp}{r}\right)^2\left(2e^{-(vt/\sigma_\parallel)^2/2} - e^{-(v/\sigma_\parallel)^2(t-r/c)^2/2} - e^{-(v/\sigma_\parallel)^2(t+r/c)^2/2}\right) \\ &- \sqrt{\frac{\pi}{2}}\frac{\sigma_\parallel\sigma_\perp t}{vc(\sigma_\parallel^2/v^2+\sigma_\perp^2/c^2)^{3/2}} e^{-t^2/2(\sigma_\parallel^2/v^2+\sigma_\perp^2/c^2)}\Bigg]\,. \end{aligned} \tag{S23}$$

Since $v \approx c$ and $\sigma_\parallel \gg \sigma_\perp$, the above equation can be further simplified as

$$\begin{aligned} B_\theta^c(0^-, r\ll\sigma_\perp, t) \approx 2\pi n_0 q r\Bigg[&\left(\frac{\sigma_\perp}{r}\right)^2\left(2e^{-(ct/\sigma_\parallel)^2/2} - e^{-(c/\sigma_\parallel)^2(t-r/c)^2/2} - e^{-(c/\sigma_\parallel)^2(t+r/c)^2/2}\right) \\ &- \sqrt{\frac{\pi}{2}}\frac{\sigma_\perp ct}{\sigma_\parallel^2} e^{-(ct/\sigma_\parallel)^2/2}\Bigg]\,. \end{aligned} \tag{S24}$$

From Eq. (S24) and expanding for small r, it follows that when the central beam slice reaches the conductor ($t = 0$), the induced magnetic field close to the axis has an amplitude

$$B_\theta^c(0^-, r\ll\sigma_\perp, 0) \approx 2\pi n_0 q r\left(\frac{\sigma_\perp}{\sigma_\parallel}\right)^2 + \mathcal{O}(r^3) \approx \left(\frac{\sigma_\perp}{\sigma_\parallel}\right)^2 B_\theta^b(0^-, r\ll\sigma_\perp, 0)\,, \tag{S25}$$

where in the last equality we used the small r expansion of Eq. (S3) and $\mathbf{B}^b = \mathbf{v}/c \times \mathbf{E}^b$. The surface magnetic field of the conductor at $t = 0$ is therefore $(\sigma_\parallel/\sigma_\perp)^2$ lower than the beam self-field. The accuracy of this approximation can be assessed for the parameters of Fig. S4. For $\omega_p\sigma_\parallel/c = 6$, $\omega_p\sigma_\perp/c = 1$, $\omega_p r/c = 0.1$ and $\omega_p t = 0$, the numerical evaluation of Eq. (S16) gives $B_\theta^c \approx 1.35\times10^{-3} m_e\omega_p/e$, close to the above formula, $B_\theta^c \approx 1.39\times10^{-3} m_e\omega_p/e$.

By expanding Eq. (S24) for small r one gets

$$B_\theta^c(0^-, r\ll\sigma_\perp, t) \approx -2\pi n_0 q r e^{-c^2t^2/2\sigma_\parallel^2}\left(\frac{\sigma_\perp^2}{\sigma_\parallel^2}\frac{c^2t^2}{\sigma_\parallel^2} + \sqrt{\frac{\pi}{2}}\frac{\sigma_\perp}{\sigma_\parallel}\frac{ct}{\sigma_\parallel} - \frac{\sigma_\perp^2}{\sigma_\parallel^2}\right)\,. \tag{S26}$$

Thus, when $t \gg r/c$ and $t \ll \sigma_\parallel^2/c\sigma_\perp$, which corresponds to the magnetostatic limit, the right-hand side of Eq. (S24) is dominated by the second term,

$$B_\theta^c(0^-, r\ll\sigma_\perp, t) \approx -\sqrt{2\pi^3} n_0 q\frac{\sigma_\perp r}{\sigma_\parallel^2}\, ct\, e^{-(ct/\sigma_\parallel)^2/2}\,, \tag{S27}$$

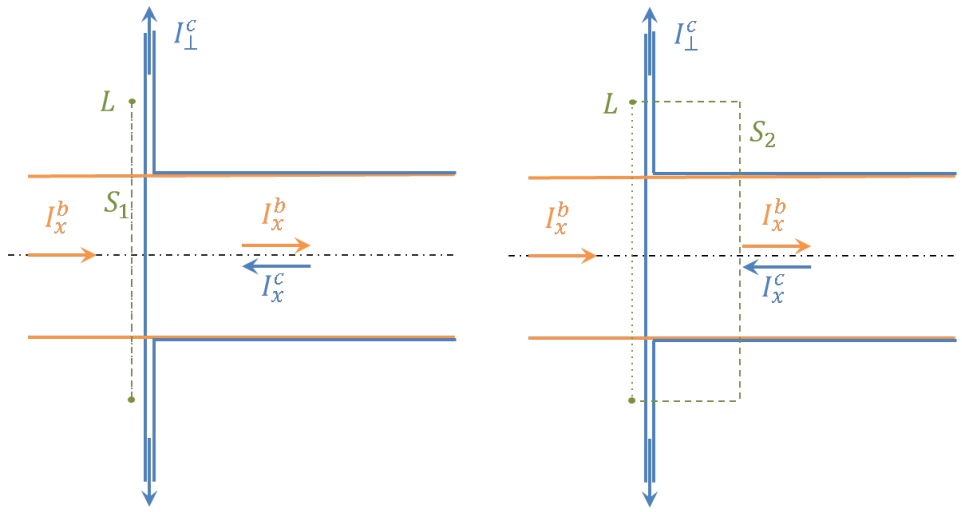

FIG. S6. Equilibrium current distributions due to a particle beam propagating into a conductor. Ampère's law is applied for two different surfaces S_1 and S_2 (dashed green curve) bounded by the loop L (dotted green line).

that is, by the evanescent modes. The above expression could have been derived more directly by neglecting $\mathcal{I}_1$ in Eq. (S18) and approximating $k_x \sim -ik_\perp$ in $\mathcal{I}_2$.

Let us now estimate the surface magnetic field generated at large radii, $r \gg \sigma_\perp$. Equation Eq. (S20) can then be approximated as

$$\mathcal{I}_2 \approx i\int_1^\infty du \frac{J_1(|\omega| ru/c)}{\sqrt{u^2-1}} = i\frac{\sin(\omega r/c)}{\omega r/c}\,. \tag{S28}$$

By substituting Eq. (S28) and Eq. (S19) in Eq. (S16), and by using Euler's formula and the trigonometric identity $2\sin^2(\omega r/2c)\cos(\omega t) - \sin(\omega r/c)\sin(\omega t) = \cos(\omega t) - \cos(\omega(t-r/c))$, one obtains

$$B_\theta^c(0^-, r\gg\sigma_\perp, t) \approx -\sqrt{8\pi} n_0 q \frac{\sigma_\parallel \sigma_\perp^2}{vr}\int_{-\infty}^{\infty} d\omega\, e^{-(\sigma_\parallel \omega/v)^2/2}\left[\cos(\omega(t-r/c)) - \cos(\omega t)\right]\,. \tag{S29}$$

By explicitly calculating the integral one gets

$$B_\theta^c(0^-, r\gg\sigma_\perp, t) \approx 4\pi n_0 q \frac{\sigma_\perp^2}{r}\left[e^{-(vt/\sigma_\parallel)^2/2} - e^{-(v/\sigma_\parallel)^2(t-r/c)^2/2}\right]\,. \tag{S30}$$

From Eq. (S30) and since $v \approx c$, it follows that when the central beam slice reaches the conductor ($t = 0$), at large radii the magnetic field of the conductor scales as

$$B_\theta^c(0, r\gg\sigma_\perp, 0) \approx 4\pi n_0 q \frac{\sigma_\perp^2}{r}\left(1 - e^{-r^2/2\sigma_\parallel^2}\right)\,. \tag{S31}$$

This implies that for $\sigma_\perp \ll r \lesssim \sigma_\parallel$, $B^c(0^-, r, 0)$ is lower than the magnetic self-field of the beam by a factor of $[1-\exp(-r^2/2\sigma_\parallel^2)]$, and that for $r \gg \sigma_\parallel \gg \sigma_\perp$, $B^c(0^-, r, 0)$ approaches the (radially decreasing) beam self-field. Interestingly, Eq. (S30) also indicates that $B_\theta^c(0^-, r\gg\sigma_\perp, t)$ changes its sign at $t = r/2c$, in agreement with Fig. S5.

Equations (S24) and (S30) demonstrate that the induced magnetic field vanishes everywhere along the conductor's surface when $\sigma_\parallel \to \infty$, that is, in the nonradiating (stationary) limit. This result can be readily understood from Fig. S6, which sketches the stationary current distribution induced in the conductor by the incoming particle beam. To ensure charge conservation, the longitudinal current induced through the beam cross-section deep inside the conductor must convert to a radial current along the conductor's boundary. Integrating the azimuthal magnetic field over a loop centered on $r = 0$ and tangential to the conductor's surface (see Fig. S6), Ampère's law tells us that

$$\int_L \mathbf{B}\cdot\mathbf{dl} = 2\pi r B_\theta(x = 0^-, r) = \frac{4\pi}{c}\int_S \mathbf{j}\cdot d\mathbf{S} \tag{S32}$$

where the surface S is bounded by the loop L, and we have neglected the displacement current as we consider the stationary regime. By choosing S as S_1 (see Fig. S6, left panel) gives

$$2\pi r B_\theta(x=0^-,r) = \frac{4\pi}{c}\int_{S_1} \mathbf{j}_x^b dS = \frac{4\pi}{c} I_x^b \,. \tag{S33}$$

This means that $B_\theta(0^-,r)$ is only due to the beam current, and conversely that the induced currents in the conductor do not create a magnetic field outside of it. An alternative picture is provided by choosing the integration surface as S_2 (see Fig. S6, right panel)

$$2\pi r B_\theta(x=0^-,r) = \frac{4\pi}{c}\left(I_x^b - I_x^c + I_\perp^c\right) \,. \tag{S34}$$

In the steady state, one has $I_x^c = I_\perp^c$, which again implies a vanishing contribution of the conductor to $B_\theta(x=0^-,r)$. We recall that Ampère's law in Eq. (S32) is valid only in the stationary case as it neglects the contribution of the displacement current. Thus, the reasoning of the stationary case does not apply to the radiating regime.

---

[1] V. Ginzburg and V. N. Tsytovich, *Transition Radiation and Transition Scattering* (Adam Hilger, Bristol, UK, 1990).

[2] I. S. Gradshteyn, I. M. Ryzhik, Alan Jeffrey, and Daniel Zwillinger, *Table of Integrals, Series, and Products* (Academic Press, Burlington, USA, 2007).

[3] V. A. Verzilov, "Transition radiation in the pre-wave zone," Phys. Lett. A **273**, 135–140 (2000).

[4] James E. Harvey, "Fourier treatment of near-field scalar diffraction theory," Am. J. Phys. **47**, 974–980 (1979).

[5] M. Castellano and V. A. Verzilov, "Spatial resolution in optical transition radiation beam diagnostics," Phys. Rev. ST Accel. Beams **1**, 062801 (1998).